A Soft Inflatable Robot Driven by Hydraulic Folded Pouch Actuators for Minimally Invasive Surgery

Jianlin Yang[1,2], Mark Runciman[2], James Avery[2], Zhijun Sun[1], and George Mylonas[2], *Member, IEEE*

Abstract—**This paper presents a soft, inflatable, cable-driven parallel robot (CDPR) for Minimally Invasive Surgery. The CDPR has 5 degrees of freedom and is driven by 6 cables and 6 hydraulic folded actuators. The actuator utilizes a folded chamber to pull a cable. The robot comprises a soft hexagonal variable-stiffness scaffold with a welded internal triangular support, which increases the stiffness of the robot when pressurized. The fabrication methodology is demonstrated in detail. A test platform is designed to obtain the characteristics of the folding actuator. The relationship between input liquid volume and actuator displacement can be predicted well by a geometry-based method. The displacement output of the actuator can reach 22 mm, which is nearly twice its length in its zero-volume folded state. Robot repeatability tests show mean and root mean square errors below 0.3 mm. The robot is made from plastic laminate sheets of thickness 120 μm and can deploy from 100 mm in length and 14 mm in diameter when folded, into an inflatable hollow hexagonal prism with 29 mm side length and 78 mm edge length. Deployment in a colon phantom is demonstrated and simulated surgery is conducted to validate the robot performance.**

Index Terms—**Soft Robotics, Hydraulic Actuators, Cable-driven Parallel Robot.**

I. INTRODUCTION

MINIMALLY Invasive Surgery (MIS) has brought many benefits to patients such as reduced trauma through smaller incisions, shorter hospital stays and recovery time, fewer post-operation complications and pain [1]. In some forms of MIS, long and rigid instruments suffering from the fulcrum effect are difficult for surgeons to use [2]. Robotic systems can solve this problem by providing more ergonomic, accurate, stable, and scaled motion. There is a trend for soft MIS instruments in recent years and both patients and surgeons express a preference for soft devices in comparison with metallic or other rigid devices [3]. Soft robots have better

adaptability and are more amiable to safer interactions with their environment. They are considered to have great potential in solving many of the challenges that conventional rigid robots are facing.

The STIFF-FLOP manipulator brought attention to soft robots in MIS, since it was designed for use in laparoscopic surgery [4]. Different soft robots for MIS have been developed, including cable-driven [5], fluid-actuated [4], [6], magnetic-actuated [7], and other actuation methods [8]. Most of these robots are based on elastomers that occupy a certain volume. Pouch motors are a type of low-profile and low-cost actuators [9]. Unlike McKibben pneumatic artificial muscles (PAM) [10], they have zero-volume when deflated and can deploy into large sizes upon inflation, which has potential applications in confined MIS situations such as a lumen.

Runciman *et al.* proposed an inflatable open-loop controlled robot for MIS driven by hydraulic pouch motors [11]. The robot is based on the CYCLOPS concept, a cable-driven parallel surgical robot, which initially had a rigid scaffold, showing high payload capabilities, high repeatability, and large workspace [12], [13]. The robot with a soft scaffold in [11] can be folded and wrapped around an endoscope, commonly referred to as an over-the-scope arrangement and be deployed in the lumen after inflation. The pouch actuators replaced the long Bowden cable mechanisms in [14] which suffered from friction and hysteresis. However, the pouch actuators are still relatively large and, additionally, displacement amplification mechanisms based on pulleys are needed to compensate for the relatively limited stroke offered by these actuators.

Existing research is focused on improving the contraction ratio (CR) of pouch motors [15]-[17]. Kwon *et al.* developed a pouch-like flat artificial muscle, which improves CR by inner constraint layers and external constraint rigid plates [15]. Xie *et al.* proposed a novel PAM based on a CR amplification mechanism composed of a vertical plate and 2 bars [16]. Oh *et al.* proposed a group of paired actuators that include series-parallel hybrid pouch motors [17]. They all significantly improved CR, but their structures and manufacturing processes are relatively complicated.

In contrast, folded actuators made of an airbag are flexible, adaptable, simple, able to generate high force and displacements, low-profile, and cheap [18]-[21]. Their volume is very small while deflated but can achieve large expansion upon inflation. They are mostly designed for soft wearable devices to assist flexion of elbow, hip, ankle, and finger joints.

Inspired by the folded actuators above, this paper proposes a soft inflatable cable-driven parallel robot (CDPR) for MIS that is driven by folded hydraulic actuators as shown in Fig. 1.

Hydraulic actuation is utilized to avoid friction associated with long Bowden cables used in [14]. The novel miniature actuator has a high stroke nearly twice the length of the actuator in its zero-volume folded state. The robot is a monolithic device integrating an effector and six folded chamber actuators used to actuate respective cables into a soft plastic prismatic scaffold. The scaffold stiffness is significantly increased by a hollow inflatable triangular support compared to the scaffold in [14]. The robot can deploy in a constrained colon phantom from a soft folded state to a high-stiffness inflatable state (Fig. 11). The actuators and the scaffold are made from flexible plastic film laminates, which are easy to fabricate and low-cost, allowing the robot to be disposable, with potential benefits for MIS applications.
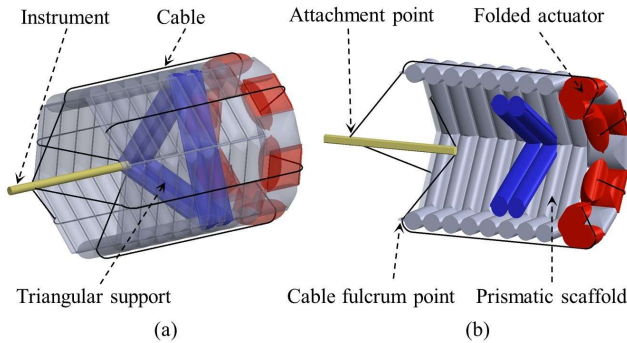

Figure 1. 3-D model of the proposed monolithic, soft, inflatable CDPR. (a) Side view. (b) Cross-sectional view.

II. SYSTEM DESCRIPTION

A. Robot system overview

Fig. 1 presents a soft inflatable CDPR for gastrointestinal surgery, which is largely made of flexible but inextensible plastic film. Six folded hydraulic actuators are welded on the scaffold, and connect to the instrument via six cables, providing five degrees of freedom (DOFs) to the CDPR. The proposed actuator produces ample displacement without the need for displacement amplification mechanisms, such as pulleys. The cable fulcrum points have a planar layout (i.e., the plane constituted by six cable fulcrum points is between two groups of cable attachment points shown in Fig. 1) replacing the spatial layout (i.e., cable attachment points are all between the two planes constituted by two groups of cable fulcrum points on the top and bottom of the prism) in [14]. For the planar layout, the longitudinal size of the scaffold can be very small (for example, 5 mm) as long as the scaffold is stable enough, which is beneficial for shortening the scaffold and facilitating robot's navigation through the colon bends. However, forces generated by cables at fulcrum points may make the scaffold deform considerably and affect the established kinematic model. To avoid this, a stable scaffold with high stiffness after inflation is achieved by means of an inflatable triangular support internally added to the structure. In terms of robot deployment, the deflated scaffold is wrapped around a carrier endoscope (over-the-scope arrangement), which delivers the robot inside a lumen. After reaching the operative site, the robot inflates and braces itself against the lumen wall (e.g., colon) and the surgery is performed. After surgery, the robot is deflated and extracted from the colon.

B. Actuator

Fig. 2(a1-a3) shows the working principle of the proposed actuator. Fig. 2(a1) shows a folded chamber with no liquid or gas in it, where one end of the chamber is connected to a cable through a small hole on the other end. Upon inflation, the folded chamber will deploy and pull on the cable. When fully deployed, the displacement of the cable is approximately equal to the chamber length. As shown in Fig. 2(b), there is an extra welding line at the end of the actuator and a flexible wire passes between it and the inflated part. A cable is tied to the wire. Fig. 2(c) shows a folded actuator made of plastic film and fabricated by a laser welding device developed in [14]. The cable is a 0.18 mm diameter fishing line (J-BRAID×8E 0.18-300MU, Japan), which can withstand a force of 118 N. Fig. 2(d-e) shows the folded actuator unfolding and pulling the cable after inflation.
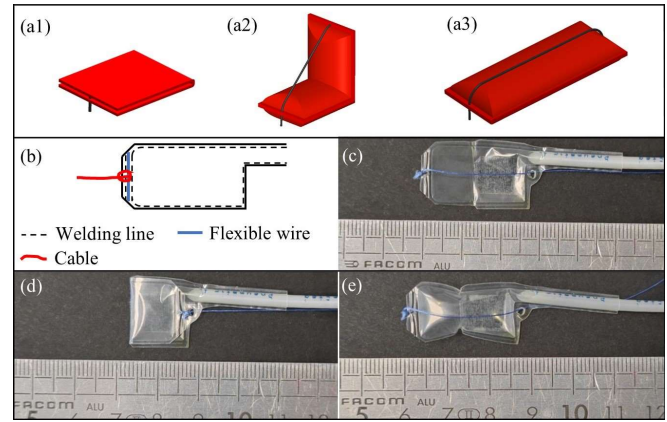

Figure 2. Actuator description. (a1-a3) Working principle of the folded actuator. (b) Diagram of the actuator. (c) An actuator manufactured by laser welding. (d-e) A folded actuator deployed into an unfolded actuator. (The ruler is showing mm.)

C. Robot fabrication

As shown in Fig. 3(a), the prismatic scaffold, the triangular support, and the actuators were individually fabricated by laser welding according to their respective welding patterns. The plastic sheet used here is a polyethylene (PE) polyethylene terephthalate (PET), solvent bonded PE/PET/PE triple laminate of thickness 30/60/30μm, which is biocompatible. The prismatic scaffold and triangular support units are each composed of interconnected chambers, so only two tubes are required for their inflation.

With reference to Fig. 3(b-c), after cutting the excess parts, the actuators were manually welded with a soldering iron at the blue welding lines in Fig. 3(a). Holes on the scaffold and the actuators for cables to pass through were made with a soldering iron. Fig. 3(d) shows the triangular support which is manually welded onto the scaffold at the red welding points in Fig. 3(a). A soldering iron was used to manually weld the edges of the scaffold at the green welding lines seen in Fig. 3(e). Since the rectangular part of the scaffold with 8×6 chambers would contract after inflation, the two edges were welded in dashed lines to enable the welded prism edge to contract upon inflation. Finally, the cables were connected to the brass tube effector as shown in Fig. 3(f).

For easy delivery through intestine bends, the scaffold needs to be as short as possible, but the actuators and cable fulcrum points need sufficient clearance from the triangular support to avoid interference. With a perimeter of 180 mm, the equivalent diameter of the robot scaffold is 57.3 mm, while the colon diameter range is 30~80 mm [22] and compliant. The actuator width is 15mm which is half of the side length of the unpressurized prismatic scaffold, as seen in Fig 3(a). Preliminary testing found that for this sized scaffold, the actuators' chamber length should be kept within 25mm to avoid collision during operation. However, the robot is fully scalable and all dimensions can be adjusted to suit different requirements.
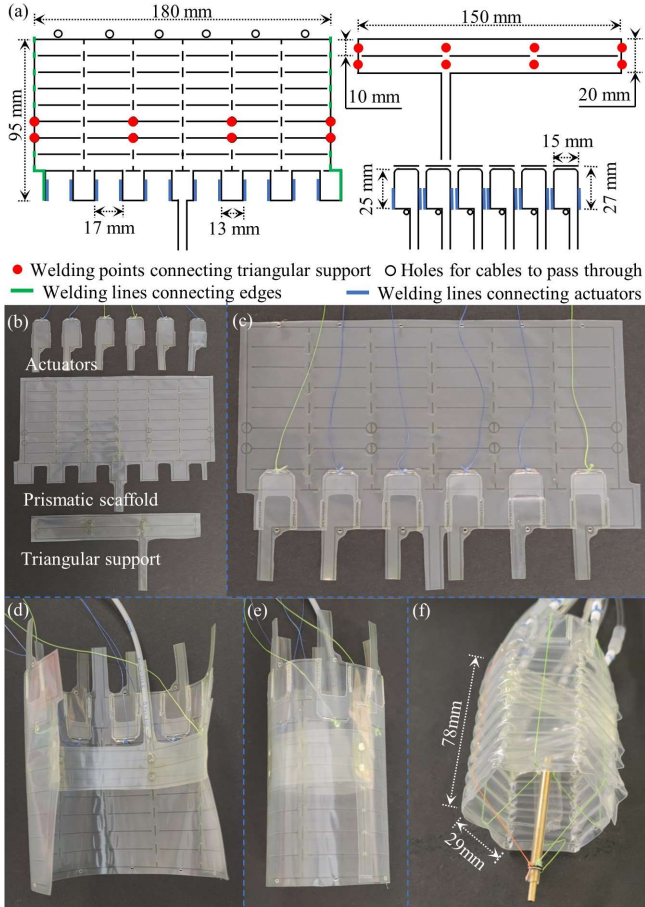

Figure 3. Robot fabrication. (a) Welding patterns for producing the scaffold layer (left), the triangular support layer (upper right), and the layer for actuators (lower right) with welding areas for their joining. (b-c) Cutting and manually welding actuators along blue lines in (a). (d) Manually welding triangular prism support according to red lines in (a) onto the hexagonal prism layer. (e) Manually welding edges along green lines in (a) to result in a cylinder shape. (f) Lastly, cables are connected to the brass tube end-effector and the robot structure can be inflated and shaped into a hollow regular hexagonal prism.

III. ACTUATOR ANALYSIS

Due to the incompressibility of liquids, the displacement of the hydraulic actuator can be controlled by the input volume of liquid. This makes open-loop control of the actuator possible. Therefore, it is necessary to study the relationship between the displacement of the hydraulic actuators and the volume of input liquid. Here we propose a geometry-based method to model this relationship. Fig. 4(a1-a3) shows three states of the folded chamber. The two on the left in Fig. 4(b-c) are the side-views of the model that approximates the geometry of the folded chamber in Fig. 4(a2-a3) respectively. The two ends of the actuator are assumed as semi-circles. For a completely inflated flat rectangular chamber, its maximum radius r_m is determined by its width. That is:

$$r_m = \frac{W_0}{\pi} \tag{1}$$

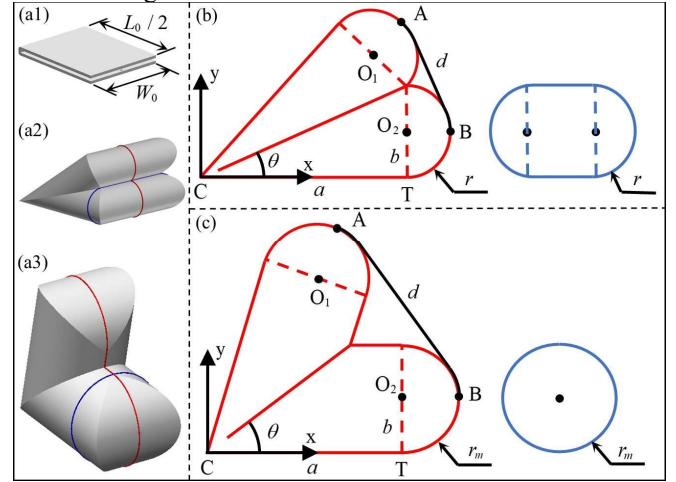where the chamber width W_0 is assumed not greater than the chamber length L_0.

Figure 4. Diagram for actuator analysis. (a1-a3) Three states of the folded chamber. (b-c) The left one is side view of the model that approximates the actuator geometry. The right one is the cross-section perpendicular to the x-axis and passing through point T. The length of the black line represents the actuator displacement.

As shown in Fig. 4(b), when the actuator inflates from zero liquid input, the shape in side-view is assumed to be composed of two right triangles and two semi-circles. Then we have:

$$r = \frac{L_0 \sin \theta}{\pi \sin \theta + 4 \cos \theta} \tag{2}$$

where θ is half of the deploying angle and r is the radius of the semi-circle. Here r is smaller than r_m. Based on symmetry, the actuator displacement d can be calculated by the cable length between A and B, including one line segment whose length is equal to the length of O_1O_2 and two arcs.

$$d = \sqrt{(b \sin 2\theta + a \cos 2\theta - a)^2 + (a \sin 2\theta - b \cos 2\theta)^2} + 2r\theta \tag{3}$$

where a is the length of CT which is equal to $(L_0-\pi r)/2$ and b is the length of O_2T which is equal to r. The area of the shape in side-view is:

$$A_s = \pi r^2 + 2ar = L_0 r \tag{4}$$

The liquid input is the volume of the actuator. The volume can be calculated by the product of the shape area in side-view and the equivalent width. Its width changes along the actuator, but here it is assumed constant, and is determined by the cross-section perpendicular to the x-axis passing through point T, as shown on the right of Fig. 1(b). Hence, the equivalent width can be calculated by the area of the cross-section divided by the height:

$$W_e = [2r(W_0 - \pi r) + \pi r^2]/2r = W_0 - \frac{\pi r}{2} \tag{5}$$

The volume of the actuator is:

$$V = A_s \cdot W_e = L_0 W_0 r - \frac{\pi L_0 r^2}{2} \tag{6}$$

The radius of the semi-circle increases as the volume of liquid injected increases. After r reaches r_m, the shape of the actuator will change. As is shown in Fig. 4(c), the shape is composed of two right-angled trapezoids and two semi-circles. A critical value for θ is θ_c, when the radius r reaches its maximum r_m and it can be calculated by (1) and (2):

$$r = r_m = \frac{W_0}{\pi} = \frac{L_0 \sin\theta}{\pi \sin\theta + 4\cos\theta} \tag{7}$$

After the radius of the semi-circle reaches this maximum, it will stay constant for the rest of the actuator stroke. However, the displacement of the cable maintains the same expression as (3). The area of the shape in side-view is:

$$A_s = 2L_0 r_m - \pi r_m^2 - \frac{4r_m^2}{\tan\theta} \tag{8}$$

The shape of the cross-section along the actuator is a circle and is shown on the right of Fig. 4(c). The equivalent width can be calculated by:

$$W_e = \pi r^2 / 2r = W_0 / 2 \tag{9}$$

The volume of the actuator is:

$$V = A_s \cdot W_e = L_0 W_0 r_m - \frac{\pi W_0 r_m^2}{2} - \frac{2W_0 r_m^2}{\tan\theta} \tag{10}$$

Finally, the displacement of the cable is:

$$d = \begin{cases} \sqrt{[r\sin 2\theta + (\frac{L_0}{2} - \frac{\pi r}{2})\cos 2\theta - (\frac{L_0}{2} - \frac{\pi r}{2})]^2 + [(\frac{L_0}{2} - \frac{\pi r}{2})\sin 2\theta - r\cos 2\theta - r]^2} + 2r\theta, & 0 \le \theta \le \theta_c \\ \sqrt{[r_m \sin 2\theta + (\frac{L_0}{2} - \frac{W_0}{2})\cos 2\theta - (\frac{L_0}{2} - \frac{W_0}{2})]^2 + [(\frac{L_0}{2} - \frac{W_0}{2})\sin 2\theta - r_m \cos 2\theta - r_m]^2} + 2r_m\theta, & \theta_c \le \theta \le \frac{\pi}{2} \end{cases} \tag{11}$$

where r, r_m and θ_c can be calculated by (2) (1), and (7). The volume of the actuator can be obtained by (6) and (10):

$$V = \begin{cases} L_0 r (W_0 - \frac{\pi r}{2}), & 0 \le \theta \le \theta_c \\ \frac{L_0 W_0^2}{\pi} - \frac{W_0^3}{2\pi} - \frac{2W_0^3}{\pi^2 \tan\theta}, & \theta_c \le \theta \le \frac{\pi}{2} \end{cases} \tag{12}$$

The objective of this section was to study the relationship between the output displacement of the actuator and the volume of input liquid. However, the explicit expression of *V(d)* would be complicated based on (11) and (12). Since *d(θ)* and *V(θ)* have been calculated, the graph of *V(d)* can be plotted using Matlab, which is shown in the next section.

IV. MECHANICAL VALIDATION

A. Characteristics of the actuator

Due to the incompressibility of liquid, a hydraulic actuator could be controlled in open-loop. Here, we use water as the hydraulic medium. A simple mechanism is designed to test the displacement of the actuator as shown in Fig. 5(a). Fig. 5(b-c) shows the 3-D model of the actuator in detail. For rigidity, the inflated chamber is laser-welded on a plastic base fixed on the bench. The cable connected to the actuator passes through a short Bowden tube and then connects to a car-like slider, on which there is a retro-reflective marker as shown in Fig. 5(a).

The cable is finally connected to a hanging weight via a pulley. There is also a fixed marker on the bench. The cable displacement is measured by calculating the distance between the moving marker and the fixed marker on the bench. Positions of the markers are tracked by the OptiTrack (NaturalPoint, USA) optical motion tracking system. Three actuators were fabricated for testing. Before tests, air bubbles in the system were all expelled.

The folded hydraulic actuator is connected to a syringe pump via a tube with an outer diameter of 3 mm and a length of 1 m. A pressure sensor (SparkFun MS5803-14BA), which is close to the syringe pump, is connected to the hydraulic circuit to measure the pressure inside the actuator. An Arduino Uno microprocessor is used to control the pump and obtain pressure sensor information.
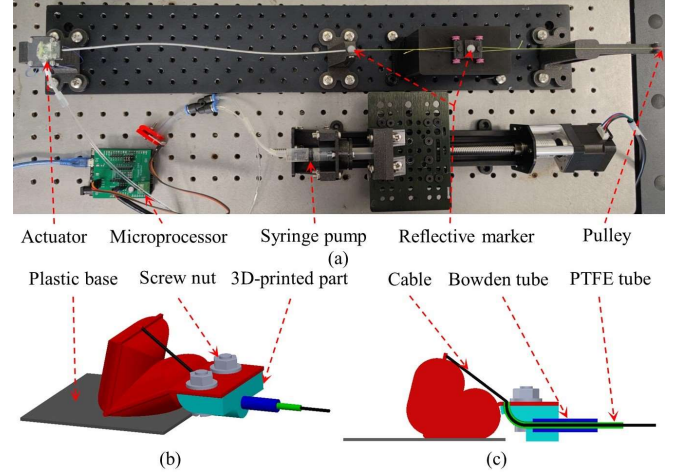

Figure 5. (a) Setup for actuator test. (b-c) Detailed drawing of the actuator.

Fig. 6(a) shows the theoretical and measured relationships between the cable displacement and the liquid input in the actuator. To tension the cable, a 50 g weight was hung on it. The curve for observed position is based on averaged measures obtained by three actuators. When the liquid volume injection range is 0-0.5 mL, the actuator is inflating but cannot generate displacement output. There exist significant errors between the theoretical position and the observed position. The theoretical liquid input and maximum displacement are greater than the measured values. One reason is that the welding lines have a width of ~0.5 mm so the actual length and width of the inflated part are approximately 24.5 mm and 14.5 mm respectively. Another reason is that a piece of plastic sheet at one end of the actuator is needed for mounting the flexible wire and attaching the cable, and it cannot pass through the hole at the other end, resulting in a displacement reduction of ~3 mm, as seen in Fig. 2(b-c). Taking these two factors into consideration, the theoretical position can be compensated, and it is much closer to the observed curve.

Fig. 6(b) shows the relationships between the cable displacement and the liquid input volume in the actuator under different payloads. The displacement of the actuator can reach more than 20 mm. When the actuator is in a large displacement, the hysteresis decreases with increasing payload. This is because when the payload is small, the chamber has a certain stiffness. Even if it is not fully filled with liquid, it still has some stiffness and is not easy to fold. To avoid excessive

hysteresis, payloads in later tests are not less than 100 g. However, a larger payload will cause larger displacement loss due to the inherent actuator flexibility.

Fig. 6(c) shows a series of hysteresis loops with different input ranges under a payload of 100 g. To make the actuators repeatable, desired crease lines were forced by folding and compressing the chamber manually during fabrication. The hysteresis decreases when the liquid input range decreases. Especially when the liquid input ranges are 0~1.2 mL and 0~1.1 mL, hysteresis decreases significantly.
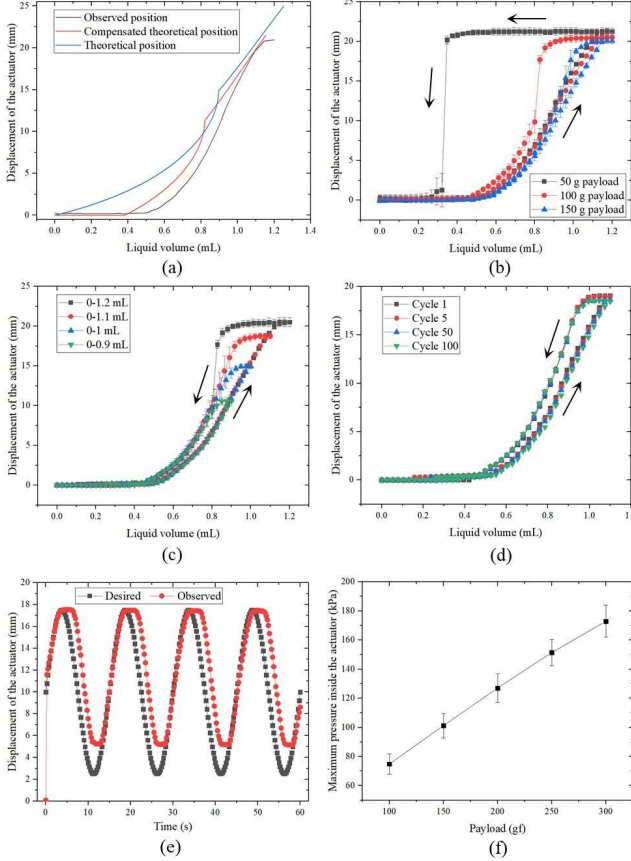

Figure 6. Characteristics of the actuator. (a) Theoretical and real actuator displacement to liquid input. (b) Actuator displacement to liquid input with different payloads. (c) Hysteresis loops with different input ranges. (d) 10-cycle repeatability results. (e) Single actuator control results in tracking sine signal. (f) Maximum pressures inside the actuator during 0~1.1 mL input to different payloads. (All the hysteresis loops are counter-clockwise and all the error bars indicate standard deviation for n=3 samples.)

Repeatability test results are shown in Fig. 6(d). One actuator was selected for test, and was driven 100 times with 0~1.1 mL input and 100 g payload. The reason for the slight curve shift, should be attributed to plastic material stretching. Open-loop control based on liquid volume was implemented by curve fitting the rising section of the 100 g loop (which is a reasonable approximation based on the level of required forces for ESD, which is clarified in Section V-C) from 0.5 to 1.1 mL in Fig. 6(b). The expression for actuator and robot control is:

$$f(x) = (1.248x^3 - 43.43x^2 + 694.5x + 4944) \times 10^{-4} \quad (13)$$

where $f(x)$ is the liquid volume, and x is the actuator displacement limited within 20 mm. Fig. 6(e) shows the tracking results of a single actuator, in which the payload is 100 g. Before the test, 0.5 mL of water was kept in the

actuator. The actuator could follow the command signal in about 0.2 seconds. Tracking errors are mainly due to actuator flexibility and friction.

Fig. 6(f) shows the maximum pressure inside the actuator across an actuation cycle with different payloads. Each test was repeated 10 times and maximum pressure in these 10 cycles was chosen. Maximum pressure inside the actuator is linear to the payload. Maximum pressure under 350 g payload is not shown as the actuator burst when the test was in the second cycle and the maximum pressure was about 200 kPa which is considered as the limit pressure.

B. Scaffold stiffness test

Variable stiffness of the scaffold can be achieved by adjusting the air pressure inside the prismatic scaffold and the triangular support. Variable stiffness is important to the proposed robot, as it should be soft enough to fold while delivered to the surgical site, and then rigidify upon deployment to achieve a stable structure ensuring the established kinematic model is valid. Fig. 7(a) shows the stiffness test setup for the robot scaffold. The scaffold was mounted between two rigid plates, one of which was fixed on a linear stage, and the other attached to a force/torque transducer (Nano 17, ATI Automation, USA) connected to a 16-bit NI USB-6259 DAQ (National Instruments, USA). Pneumatic supply was provided by an air pump (OF302-4 B, JUN-AIR, Inc., USA). The pressure inside the prismatic scaffold and the triangular support were tuned by two pressure regulators (PRE1-U08, AirCom, Germany) independently. The force sensor was brought into contact with one side of the scaffold and gradually compressed against the scaffold by 2mm to collect the initial force data. Then, the sensor compressed against the scaffold by a further 4mm and retracted to the start position after collecting force data. This process was repeated four times and the mean of the four samples was used for calculating the radial stiffness.
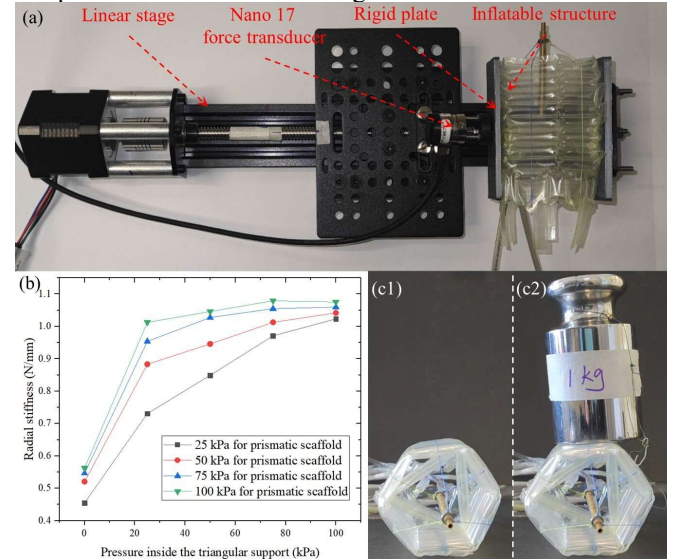

Figure 7. Stiffness test. (a) Stiffness test setup. (b) Variable stiffness test results. (c) Inflatable structure under a 1kg weight payload demonsrating no buckling.

Stiffness test results are shown in Fig. 7(b). The triangular support can significantly improve the inflatable scaffold stiffness even at a low pressure of 25 kPa. By continuing to increase the pressure, the stiffness of the scaffold slowly increased. Increasing the pressure inside the prismatic scaffold can also further increase its stiffness. A 50 kPa pressure inside the triangular support and the prismatic scaffold can provide stiffness of 0.97 N/mm, which is significantly higher than the structure stiffness of 0.38 N/mm in [14] under the same conditions. This allows the inflatable structure to work under relatively low-pressure conditions, which is considered safer and ensures material durability during long surgery sessions. In Fig. 7(c1-c2), a 1 kg weight was put on the scaffold inflated at 50 kPa, resulting in unobservable deformation. The burst pressure for the scaffold and the triangular support are about 270 kPa. On the other hand, very low pressures (e.g., < 50 kPa) cannot ensure adequate scaffold stiffness at the cable fulcrum points, and would invalidate the kinematic model of the robot.

C. Workspace of the robot

The workspace of the robot is evaluated via simulations and experiments. Fig. 8 shows the simulated workspace, in which the maximum displacement of each actuator was 20 mm, which is determined by the test data under 100 g payload in Fig. 6(b). The length of the effector is 50 mm and the distance between the two groups of attachment points is 40 mm. The hexagon formed by six feed points has a side length of 25mm which is from size measurement of the robot. Results show that the tip workspace of the robot can reach 50 mm along the X axis, 40 mm along the Y axis, and 30 mm along the Z axis. The workspace is not symmetric in the X axis due to the arrangement of cables being asymmetric, as seen in Fig. 8(c).
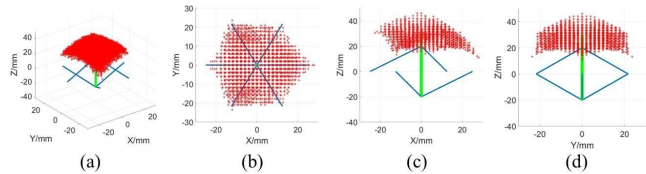

Figure 8.   Simulated tip workspace via Matlab. (a) Side view. (b) X-Y plane view. (c) X-Z plane view. (d) Y-Z plane view. (The green line is the effector and the blue lines are cables.)

Fig. 9(a-f) shows the inflated robot in different poses. The measured tip workspace is 40 mm along the X axis, 32 mm along the Y axis, and 26 mm along the Z axis. The observed workspace is smaller than the simulated due to friction in the system. Colon tumor sizes typically range between 6.2 mm to 43.6 mm [23], while the robot can operate within a 25mm workspace. The robot workspace could be extended by using actuators with larger strokes, but care should be taken to ensure they won't collide when actuating. Additionally, repositioning the robot by means of its host endoscope, or by implementing a prismatic joint in the end-effector overtube would also increase the workspace.

V. OPERATIONAL PERFORMANCE

A. Repeatability Test

Fig. 10(a) shows the setup for robotic tracking, with one side of the scaffold shown fixed to the test frame. The control system includes six syringe pumps and two Arduino mega2560 boards, controlled by a laptop over USB. Each Arduino board controls three stepper motors to drive the syringe pumps. Rigid bodies with four retroreflective markers were fixed onto the test frame and the tip of the effector.
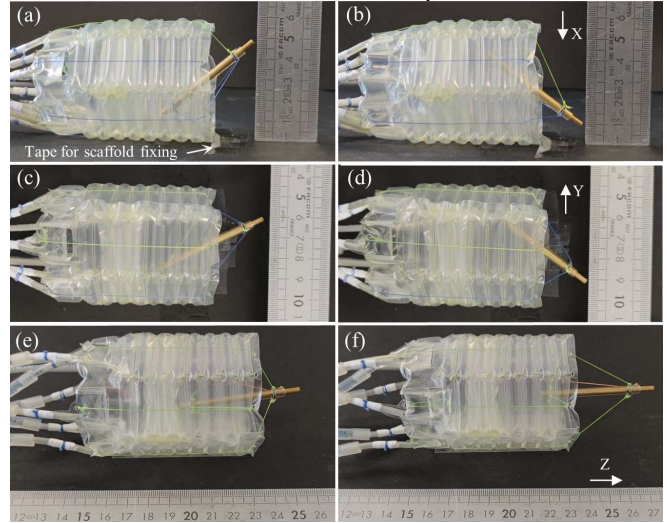

Figure 9.   The robot workspace measurement along (a-b) X axis, (c-d) Y axis, and (e-f) Z axis.
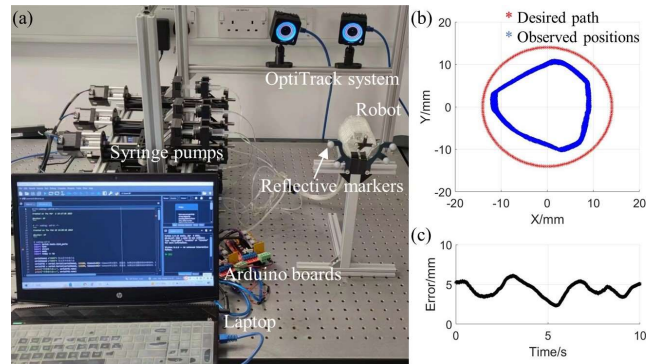

Figure 10. Robot tracking. (a) Robot system setup. (b) Tracking results. (c) Tracking errors.

TABLE I.   REPEATABILITY TEST RESULTS

	Maximum	Mean	RMSE
Error X /mm	1.0493	0.1720	0.1996
Error Y /mm	0.6882	0.1432	0.1657
Error Z /mm	0.6881	0.0891	0.1060
Absolute error /mm	1.2124	0.2630	0.2942

Fig. 10(b) shows the results of open-loop scanning of a 28 mm diameter circular path in the X-Y plane. The tracking was repeated for 10 cycles and the results of 0.5 to 9.5 cycles are shown for clarity. Fig. 10(c) shows the tracking errors over one cycle, with a mean, maximum and standard deviation of 4.35 mm, 6.12 mm and 4.44 mm respectively. Repeatability was tested by comparing each point to the average value of nine corresponding points in 9 cycles. Table I shows the maximum, mean, and root mean square errors (RMSE) of repeatability test results, with mean and RMSE smaller than 0.3 mm. The tracking error may be caused by flexibility of the

actuators and friction in the system. A triangular trajectory shape was observed as the robot approaches its singular configurations at the boundaries. Moreover, the expression for actuator control is based on a test setup that does not totally reflect its actual working scenario on the robot scaffold, which may also introduce slight errors.

B. Collapsibility and deployment

Fig. 11(a-b) shows robot deployment from its collapsed and folded state without constraints and external payloads. The overall length of the folded scaffold is ~100 mm, while its diameter is approximately 11 mm, mostly contributed by the currently incompressible end effector with a 6 mm diameter. Scaffold diameter of its proximal end is ~14 mm, mostly contributed by the tubes used for inflation and actuation. The end effector protrudes by 30 mm from the scaffold opening. After inflation, the soft scaffold deploys into a hollow hexagonal prism with a length of 78 mm, and a bottom side length of 29 mm. In surgical tasks, the robot should be able to deploy in a confined space such as the colon, which is normally collapsed. The scaffold is currently inflated with air, but a hydraulic version is also possible, with the main difference being the higher weight. Fig. 11(c-f) shows the ability of the robot to fully deploy to a regular hexagonal prism inside colon phantoms with 180 mm inner perimeter while unstretched, which is equal to the perimeter of the deployed scaffold. The triangular support provides high stiffness, which ensures the actuators do not collide when actuating.
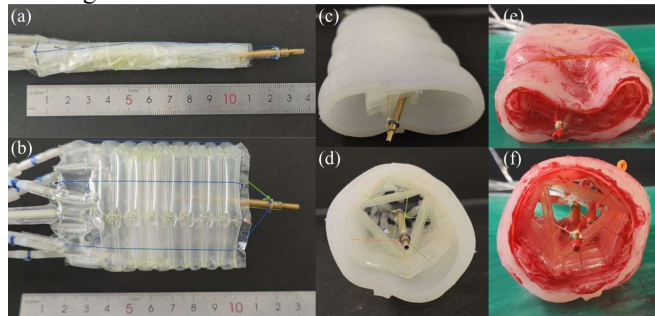

Figure 11. Robot deployment. The robot can deploy (a-b) freely from a folded cylinder to an unfolded inflatable hexagonal prism, (c-d) in a colon phantom, and (e-f) in a lubricated colon phantom constrained by rubber bands to simulate a peristaltic force.

To imitate the real colon, lubricant was applied inside and outside the colon phantom to simulate mucus. Two rubber bands were nested around the phantom to generate additional external forces, which would hinder robot deployment as in a real case. Despite these external forces the robot deployed successfully into its hexagonal prism shape. After deployment, the outer perimeter of the colon phantom had increased from 211 mm to 219 mm, demonstrating the ability of the scaffold to overcome external forces exerted on it by a collapsed colon. Each of the rubber bands when stretched to 219 mm perimeter provides 2.5 N elastic force which was measured by a spring gauge. The equivalent pressure p distributed on the soft scaffold can be calculated by the pressure formula for cylindrical containers:

$$F_r = pbd \qquad (14)$$

where F_r is the force on the radial section of the container, i.e., the elastic force of the rubber bands. b is the height of the container, i.e., the length of the inflatable structure. d is the diameter of the container, and here corresponds to the rubber band perimeter. The pressure exerted by the rubber bands on the structure is converted into a uniformly distributed equivalent pressure p of 1.12 kPa.

C. Force exertion of end-effector

Fig. 12(a) shows the end-effector force exertion test platform. The robot scaffold was fixed on the bench using double-sided tape. The end-effector was clamped to the surface of the force/torque transducer. As shown in Fig. 13(a), a Geomagic Touch haptic device (3D Systems, USA) was used to control the robot to conduct this test. The three translational DOFs and the two rotational DOFs of the end effector, correspond with that of the haptic device. Force data was measured when the haptic device was moved through its entire motion range, which is a 28 mm diameter sphere in simulated workspace after mapping to the end-effector. Fig. 12(b) shows the collected data. The difference between maximum forces in the positive and negative X axis is significant due to asymmetric arrangement of the cables as shown in Fig. 8(c). As shown in Table II, the maximum forces in each axis are all greater than 0.4 N, which is reported as the nominal force required to perform endoscopic submucosal dissection (ESD) in the colon [24]. The maximum force magnitude was 1.50 N.
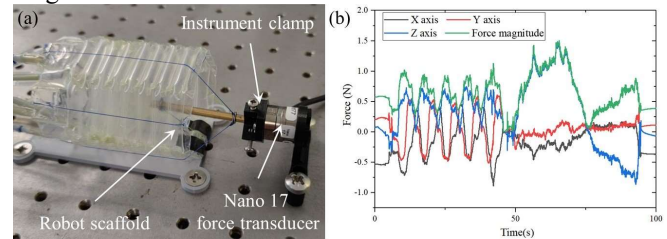

Figure 12. End-effector force exertion test. (a) Test platform. (b) Force exertion by the instrument.
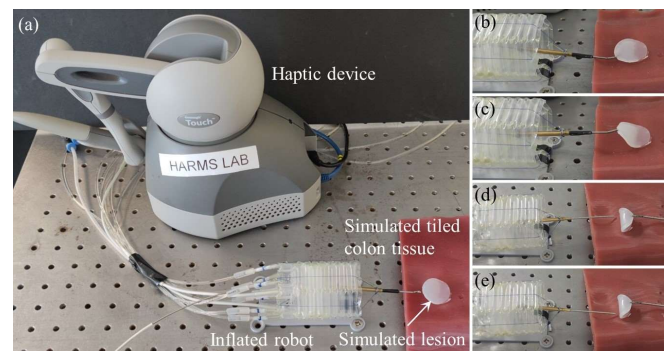

Figure 13. Simulated surgical operations. (a) Experimental setup. (b-c) Lifting the simulated lesion. (d-e) "Sweep" motion to simulate a diathermy to dissect tissues.

TABLE II.   MAXIMUM FORCES MEASURED IN EACH AXIS

Direction	+X	-X	+Y	-Y	+Z	-Z
Force /N	0.46	0.89	0.61	0.51	1.46	0.86

D. Simulated surgical tasks

As shown in Fig. 13(a), a circular silicone piece simulating a lesion approximately 27 mm in diameter was glued onto a simulated colon affixed to a workbench. A flexible endoscopic grasper was accommodated through the working channel of the end effector. Opening and closing of the grasper jaws is performed manually, as it is commonly done. Fig. 13(b-c) demonstrates the robot's ability to grasp and lift the simulated tissue flap. Fig. 13(d-e) shows the robot executing a "sweeping" motion to demonstrate its ability to guide a flexible diathermy instrument, commonly used in ESD to separate the mucosa from the submucosa and dissect the lesion.

VI. DISCUSSION AND CONCLUSION

This paper presents a soft, variable stiffness inflatable robot, driven by hydraulic folded actuators and cables in a parallel arrangement. The proposed novel miniature hydraulic actuator is easy to fabricate, low-profile, low-cost, and offers large stroke in a confined space. Robot performance was tested in terms of workspace, scaffold stiffness, ability to deploy inside a lumen, force exertion, and simulated surgical operations, demonstrating its potential for MIS applications. The robot is open-loop controlled by regulating the volume of the liquid inside the actuators. No breaking of the robot was observed during hours of tests, supporting its durability during long procedures.

Pre-clinical validation using exhumed animal tissues is ongoing to investigate several operational aspects of the system, including appropriate strategies for robot introduction and extraction from the colon. Technical work focuses on further improving open-loop control accuracy, although during surgery the physician is able to compensate for small positional errors using manual corrections. However, closed-loop control strategies are also under implementation, based on our work on soft structures shape estimation and proprioception, using Electrical Impedance Tomography (EIT) techniques [25].

Boasting soft structures, the proposed system can be considered inherently safe. In the event of a catastrophic failure of the scaffold or actuators, the air volume and pressure in the structure are small, and the small amount of liquid will not expand in volume. Investigations will culminate in *in vivo* animal studies under realistic conditions and surgical tasks.

VII. REFERENCES

[1] R. H. Taylor, N. Simaan, A. Menciassi and G. -Z. Yang, "Surgical Robotics and Computer-Integrated Interventional Medicine [Scanning the Issue]," in Proceedings of the IEEE, vol. 110, no. 7, pp. 823-834, July 2022.

[2] P. L. Anderson, R. A. Lathrop, and R. J. Webster Iii, "Robot-Like Dexterity Without Computers and Motors: A Review of Hand-Held Laparoscopic Instruments with Wrist-Like Tip Articulation," Expert Review of Medical Devices, pp. 661-672, 2016.

[3] M. Runciman, A. Darzi, and G. P. Mylonas, "Soft Robotics in Minimally Invasive Surgery," *Soft Robot,* vol. 6, pp. 423-443, Aug 2019.

[4] M. Cianchetti et al., "STIFF-FLOP surgical manipulator: Mechanical design and experimental characterization of the single module," 2013 IEEE/RSJ International Conference on Intelligent Robots and Systems, Tokyo, Japan, 2013, pp. 3576-3581.

[5] T. Deng et al., "Development of a new cable-driven soft robot for cardiac ablation," 2013 IEEE International Conference on Robotics and Biomimetics (ROBIO), Shenzhen, China, 2013, pp. 728-733.

[6] L. Manfredi, E. Capoccia, G. Ciuti, and A. Cuschieri, "A Soft Pneumatic Inchworm Double balloon (SPID) for colonoscopy," *Sci Rep,* vol. 9, p. 11109, Jul 31 2019.

[7] G. Pittiglio *et al.*, "Magnetic Levitation for Soft-Tethered Capsule Colonoscopy Actuated with a Single Permanent Magnet: A Dynamic Control Approach," in IEEE Robotics and Automation Letters, vol. 4, no. 2, pp. 1224-1231, April 2019.

[8] J. Zhu et al., "Intelligent Soft Surgical Robots for Next-Generation Minimally Invasive Surgery," Advanced Intelligent Systems, vol. 3, p. 2100011, 2021.

[9] R. Niiyama, D. Rus and S. Kim, "Pouch Motors: Printable/inflatable soft actuators for robotics," 2014 IEEE International Conference on Robotics and Automation (ICRA), Hong Kong, China, 2014, pp. 6332-6337.

[10] C.-P. Chou and B. Hannaford, "Measurement and modeling of McKibben pneumatic artificial muscles," IEEE Transactions on robotics and automation, vol. 12, pp. 90-102, 1996.

[11] M. Runciman, J. Avery, A. Darzi, and G. Mylonas, "Open Loop Position Control of Soft Hydraulic Actuators for Minimally Invasive Surgery," Applied Sciences, vol. 11, p. 7391, 2021.

[12] G. P. Mylonas et al., "CYCLOPS: A versatile robotic tool for bimanual single-access and natural-orifice endoscopic surgery," 2014 IEEE International Conference on Robotics and Automation (ICRA), Hong Kong, China, 2014, pp. 2436-2442.

[13] T. J. C. O. Vrielink, M. Zhao, A. Darzi and G. P. Mylonas, "ESD CYCLOPS: A New Robotic Surgical System for GI Surgery," 2018 IEEE International Conference on Robotics and Automation (ICRA), Brisbane, QLD, Australia, 2018, pp. 150-157.

[14] M. Runciman et al., "Deployable, Variable Stiffness, Cable Driven Robot for Minimally Invasive Surgery," Front Robot AI, vol. 6, p. 141, 2019.

[15] J. Kwon, S. J. Yoon and Y. -L. Park, "Flat Inflatable Artificial Muscles With Large Stroke and Adjustable Force– Length Relations," in IEEE Transactions on Robotics, vol. 36, no. 3, pp. 743-756, June 2020.

[16] D. Xie, J. Liu and S. Zuo, "Pneumatic Artificial Muscle With Large Stroke Based on a Contraction Ratio Amplification Mechanism and Self-Contained Sensing," in IEEE Robotics and Automation Letters, vol. 6, no. 4, pp. 8599-8606, Oct. 2021.

[17] N. Oh et al., "Design of Paired Pouch Motors for Robotic Applications," Advanced Materials Technologies, vol. 4, p. 1800414, 2019.

[18] H. D. Yang et al., "A Soft Inflatable Wearable Robot for Hip Abductor Assistance: Design and Preliminary Assessment," 2020 8th IEEE RAS/EMBS International Conference for Biomedical Robotics and Biomechatronics (BioRob), New York, NY, USA, 2020, pp. 692-699.

[19] J. Chung et al., "ExoBoot, a Soft Inflatable Robotic Boot to Assist Ankle During Walking: Design, Characterization and Preliminary Tests," 2018 7th IEEE International Conference on Biomedical Robotics and Biomechatronics (Biorob), Enschede, Netherlands, 2018, pp. 509-516.

[20] C. T. O'Neill et al., "Unfolding Textile-Based Pneumatic Actuators for Wearable Applications," Soft Robot, vol. 9, pp. 163-172, Feb 2022.

[21] L. Ge et al., "Design, modeling, and evaluation of fabric-based pneumatic actuators for soft wearable assistive gloves," Soft robotics, vol. 7, pp. 583-596, 2020.

[22] Alazmani et al., "Quantitative assessment of colorectal morphology: Implications for robotic colonoscopy." Medical engineering & physics, vol. 38, no. 2, pp. 148-154, 2016.

[23] Repici, A., et al. "Efficacy and safety of endoscopic submucosal dissection for colorectal neoplasia: a systematic review." Endoscopy, vol. 44, no. 02, pp. 137-150, 2012.

[24] J. Gafford et al., "Snap-on robotic wrist module for enhanced dexterity in endoscopic surgery," 2016 IEEE International Conference on Robotics and Automation (ICRA), Stockholm, Sweden, 2016, pp. 4398-4405.

[25] J. Avery, M. Runciman, A. Darzi and G. P. Mylonas, "Shape Sensing of Variable Stiffness Soft Robots using Electrical Impedance Tomography," 2019 International Conference on Robotics and Automation (ICRA), Montreal, QC, Canada, 2019, pp. 9066-9072.